Acta Crystallographica Section A
Foundations of Crystallography
ISSN 0108-7673

Received 5 March 2012
Accepted 12 July 2012

Keyhole electron diffractive imaging (KEDI)

Liberato De Caro,[a]* Elvio Carlino,[b] Fabio Alessio Vittoria,[a] Dritan Siliqi[a] and Cinzia Giannini[a]

[a]Istituto di Cristallografia – Consiglio Nazionale delle Ricerche (IC–CNR), via Amendola 122/O, I-70125 Bari, Italy, and [b]IOM CNR Laboratorio TASC, Area Science Park – Basovizza, Bld MM SS 14, 34149 Trieste, Italy. Correspondence e-mail: liberato.decaro@ic.cnr.it

Electron diffractive imaging (EDI) relies on combining information from the high-resolution transmission electron microscopy image of an isolated kinematically diffracting nano-particle with the corresponding nano-electron diffraction pattern. Phase-retrieval algorithms allow one to derive the phase, lost in the acquisition of the diffraction pattern, to visualize the actual atomic projected potential within the specimen at sub-ångström resolution, overcoming limitations due to the electron lens aberrations. Here the approach is generalized to study extended crystalline specimens. The new technique has been called keyhole electron diffractive imaging (KEDI) because it aims to investigate nano-regions of extended specimens at sub-ångström resolution by properly confining the illuminated area. Some basic issues of retrieving phase information from the EDI/KEDI measured diffracted amplitudes are discussed. By using the generalized Shannon sampling theorem it is shown that whenever suitable oversampling conditions are satisfied, EDI/KEDI diffraction patterns can contain enough information to lead to reliable phase retrieval of the unknown specimen electrostatic potential. Hence, the KEDI method has been demonstrated by simulations and experiments performed on an Si crystal cross section in the [112] zone-axis orientation, achieving a resolution of 71 pm.

© 2012 International Union of Crystallography
Printed in Singapore – all rights reserved

1. Introduction

Coherent diffractive imaging (CDI) is a rather novel technique to image crystalline and non-crystalline matter from nanometric down to sub-ångström resolution. It has been used, in the last decade, with X-rays (Miao *et al.*, 1999; Nugent, 2010, and references therein) and, more recently, also with electrons (so-called electron diffractive imaging, EDI) (Zuo *et al.*, 2003; Huang *et al.*, 2009; De Caro *et al.*, 2010) in a transmission electron microscope. In principle, if the intensity and phase of a diffraction pattern are known, it is possible to obtain the image of the diffracting object by their inverse Fourier transform. Unfortunately, phases are lost in the experimental diffraction pattern (the well known phase problem) and hence at least half of the information necessary to image the object is lost. If we consider an isolated object we can recover the phase information by oversampling the measured diffraction pattern at a suitable frequency. This is equivalent to an *a priori* knowledge of as many zero scattering points in the object space as the unknown phases in the Fourier space, to compensate for their loss in the measured diffraction pattern and to construct a system of equations with an equal number of unknowns.

More generally, Abbey *et al.* (2008) demonstrated, for CDI experiments performed with X-rays, that the CDI approach requires that the diffracted waves, emitted by any object, have to be scattered from a spatial region of finite size named the 'support'. The support is hence defined as the space *loci* where the scattering function is different from zero and could be an isolated object or a portion of an extended object illuminated by a confined probe. This technique with confined probes on extended objects was named keyhole CDI (Abbey *et al.*, 2008). However, in any diffraction experiment some intensities are lost due to imperfection/saturation of the detectors or to a low signal-to-noise ratio. This further lack of information can be compensated by *a priori* information on the diffracting specimen. A strong piece of *a priori* information is knowledge of the finite support. For example, in a CDI experiment with X-rays, the Fresnel diffraction configuration allows one to directly estimate the support and hence phase recovery can be safely performed (Abbey *et al.*, 2008). On the contrary, in Fraunhofer geometry the lack of reliable *a priori* information on the support places strong limitations on a successful phase reconstruction (Williams *et al.*, 2006). In fact, Fraunhofer X-ray diffraction geometry usually prevents one from measuring low-angle scattering-vector diffraction data, as they are cut away by the beam stopper used to avoid the detector damage induced by the high intensity of the direct incident beam. This lost low-angle diffraction data would contain the low-resolution image shape information about the support. Therefore, when using Fraunhofer geometry in X-ray CDI experiments, support information is missing both in the real

and in the Fourier space. This double lack of information, together with the lack of perfect spatial coherence of the incident waves and the presence of noise in the measured diffraction patterns, make the phasing process of X-ray Fraunhofer CDI data particularly difficult, leading to very slow convergence speed towards the solution that often can only be partially retrieved (Xiao & Shen, 2005; Williams *et al.*, 2007; Whitehead *et al.*, 2008).

As already mentioned, CDI can also be performed with electrons in a transmission electron microscope to determine the phases of the diffracted Bragg beams from nanometric objects under experimental conditions favouring kinematical scattering of electrons, as done on carbon nanotubes (Zuo *et al.*, 2003) or on nano-crystals (Huang *et al.*, 2009; De Caro *et al.*, 2010). Electrons are charged particles and the use of the illumination system of a transmission electron microscope allows a high degree of flexibility in the setup of the experimental conditions for CDI in Fraunhofer geometry. As long as the coherent diffraction experiment is performed in an electron microscope, good knowledge of the support is straightforwardly obtained. These data compensate for the lack of information due to the presence of the beam stopper in the Fraunhofer diffraction pattern obtained by transmission electron microscopy (TEM) and, more generally, the lack of information due to the noise of the experimental diffraction data. In fact, in the case of a thin object, the high-resolution transmission electron microscopy (HRTEM) image can directly yield knowledge of the specimen electrostatic potential projected in the plane of view (Van Dyck, 1992). This knowledge is relatively limited in resolution, due to the electron lens aberration, being well above the diffraction limit. For example, the HRTEM image resolution at optimum defocus achievable in a high-quality 200 keV microscope is 190 pm, whereas the electron wavelength, and hence the diffraction-limited resolution, is 2.5 pm (Carlino, 2008). Since high-resolution information about the electrostatic potential is available in the diffraction pattern, but only in modulus and without any phase knowledge, the EDI approach combines the HRTEM image information (object support and low-resolution object projected electrostatic potential) with the electron diffraction pattern to realize a dual-space phase reconstruction. In practice, the EDI phasing approach aims to extend the low-resolution potential information already contained in the HRTEM image up to the maximum spatial resolution corresponding to the highest Miller-index diffraction spots measured – with sufficient accuracy – in the electron diffraction pattern. Thus, EDI is not an *ab initio* phasing process as the *ab initio* term usually denotes a phasing process in which no *a priori* information in real space about the scattering object is available. Instead, the EDI approach aims to extend phase information from lower to higher resolution, and it has been shown that, through suitable data combination and phasing algorithms, sub-ångström resolution can be achieved (Huang *et al.*, 2009; De Caro *et al.*, 2010).

So far EDI has only been demonstrated for isolated nanoparticles. In the present work, we demonstrate by simulations and experiments the generalization of the EDI method in a transmission electron microscope to extended crystal specimens. The goal is achieved by properly limiting the electron beam on a nanometre range to study the specimen structure at sub-ångström resolution on a well defined nanometre-sized area. This approach can be applied to experiments performed in standard transmission electron microscopes, allowing spatial resolutions comparable to those achievable in spherical-aberration-corrected equipment. In analogy with the work on X-rays by Abbey *et al.* (2008), this approach was named *keyhole* electron diffractive imaging (KEDI).

In the first part of the paper we prove by numerical simulations on synthetic KEDI data the possibility of solving the phase problem in the case of extended crystalline samples, illuminated by a finite-sized nano-beam, when the whole diffraction pattern is not known (see §2).

In the second part of the paper (see §3) we present an experimental 'proof of concept' for KEDI. As a case study, a silicon crystal cross section prepared in ⟨112⟩ geometry, a benchmark for image resolution, was studied by a field emission gun JEOL transmission electron microscope 2010 UHR operating at 200 keV, phasing the KEDI diffraction data at about 71 pm, about three times better than the resolution of the relevant HRTEM image (190 pm) limited by the electron-lens aberrations. We also show that the method is relatively robust with respect to the electron dynamical diffraction.

Finally, some basic theoretical points of the EDI/KEDI phase problem are explored in depth in specific appendices. In Appendix *A*, we discuss the influence of the lack of information from in between the Bragg-diffracted beams when we study a crystalline specimen. In Appendix *B* we discuss in more detail this aspect applying the generalized sampling theorem (Papoulis, 1977, 1986). In Appendix *C* we discuss the role of the complex scattering function in phasing EDI/KEDI diffraction patterns. In Appendix *D* we discuss the coherence properties of a nano-sized electron beam, as used in a KEDI experiment.

2. Theoretical simulations

The diffracted intensities of a crystalline specimen illuminated by a small electron beam are mainly located at the Bragg nodes and the intensities in between the reciprocal-lattice nodes are very weak and often experimentally buried in the detector noise. In Appendices *A* and *B* we demonstrate – by using the generalized sampling theorem – that suitable oversampling ratios could completely compensate for the lost information both of weaker intensities and phases.

Moreover, the possibility of knowing *a priori* the object support and the low-resolution phases of the scattering function from the HRTEM image allows phase information extension from low to high spatial resolution, instead of a true *ab initio* phasing process. In this respect it is important to remember that, in a weak phase object approximation, the contrast of real experimental HRTEM images is inverted with respect to the projected potential, being the contrast influenced by the contrast transfer function (CTF) related to the spherical aberration and defocus (Spence, 2003). The effects

of defocus and aberrations on the image contrast can be evaluated and corrected (Zuo, 1995, p. 94). However, in addition an approximate estimation of low-resolution phases, by taking into account only the inversion of contrast in the HRTEM, without any evaluation of the CTF, is already sufficient to succeed in EDI phase extension at higher spatial resolution, as shown by Huang *et al.* (2009) and De Caro *et al.* (2010). All the above elements indicate that EDI/KEDI phase problems could have a reliable solution.

In order to verify this point, also with numerical examples, and to check the limits of the approach, in this section we simulate the results of a KEDI experiment in a transmission electron microscope for an Si structure in the [112] zone axis. The starting input image (the model) for the KEDI phasing simulation is shown in Fig. 1(*a*). We considered the Si crystal potential in [112] projection (the sample illuminated area), surrounded by a square black area representing the whole detector with an oversampling ratio $S = 9.4$ (see Appendix *A*).

Here, we have neglected the very small imaginary contribution to the crystal potential, as discussed in Appendix *C*, and assumed a real-object constraint, valid for weak phase objects (Huang *et al.*, 2007). The support is calculated in a

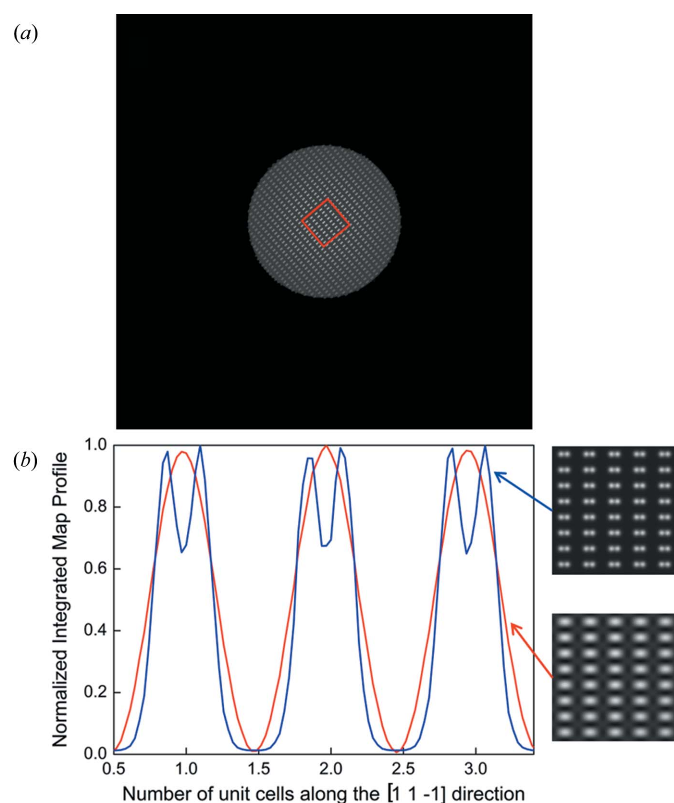

Figure 1
(*a*) Simulated potential map of an Si crystal in the [112] zone axis illuminated by a nanometre-sized electron beam. (*b*) A zoom inside the red square of (*a*) has been rotated to show horizontal profiles along the $[11\bar{1}]$ crystallographic direction (blue curve). The two Si diamond-structure sublattices, separated by 78 pm, are clearly shown at the spatial resolution of the map (58 pm). In comparison, the same portion of the map has been calculated at a 190 pm resolution (red curve), to simulate the projected potential as seen in an HRTEM image. The two Si sublattices are now not resolved.

static configuration, without any updating during the phasing process, considering null the diffracted intensities out of the illuminated area. In this regard, an important point needs to be clarified about the *exact a priori* knowledge of the support as derived by HRTEM. First of all, let us note that the evaluation of the support, starting from the HRTEM image, is almost coincident with the support directly calculated by the model. In fact, the correlation between the two supports, the first obtained by the model at 58 pm and the second by the synthetic HRTEM image at 190 pm, is larger than 99.8%. The residual difference can be ascribed to the definition of the support border and hence we assumed a shell of about 3 pixels of support border indetermination. This shell can be calculated by applying the following procedure: (i) the binary support $S1$ is calculated thresholding the HRTEM image; (ii) $S1$ is dilated by 1–2 pixels, obtaining $S_{\rm max}$; (iii) $S1$ is eroded by 1–2 pixels, obtaining $S_{\rm min}$; (iv) $S_{\rm b} = S_{\rm max} - S_{\rm min}$ gives the border shell, a few pixels large; (v) a Gaussian smoothing (1 pixel width) is applied to $S_{\rm b}$. This procedure allows us to take into account the indetermination in the support knowledge during phasing, as will be explained in the following paragraph.

A zoom inside the red square of Fig. 1(*a*) has been rotated to show horizontal profiles along the $[11\bar{1}]$ crystallographic direction (blue curve). The two Si diamond-structure sublattices, separated by 78 pm, are clearly shown at the spatial resolution of the map (about 58 pm). The spatial resolution of the map can be estimated by the FWHM of the Gaussian functions fitting the projected atomic column peaks. The same portion of the map has been calculated neglecting all Bragg-diffracted intensities beyond the 190 pm resolution (red curve), to simulate the HRTEM image of a microscope operated at 200 kV and with an objective-lens spherical aberration coefficient of 0.5 mm. In this case the Si dumbbells are not resolved due to the lens aberration.

In order to simulate the KEDI experiment we should perform the phasing process by using the modulus of the Fourier transform (FT) of the model map shown in Fig. 1(*a*) as a constraint in Fourier space (representing the KEDI diffraction pattern), and the support calculated from the 190 pm-resolution map (representing the HRTEM map) in real space. Moreover, as a starting phase set we could use both random phase sets and the phase set obtained by the FT of the HRTEM map.

In order to verify what happens if the whole KEDI diffraction pattern is not available, a modified diffraction map (modulus of the FT of the model) was produced containing, everywhere in the 1024 × 1024 pixels, zero values apart from only 1% of the higher moduli in the neighbourhood of the reciprocal-lattice nodes, as shown in Fig. 2(*a*). This setup simulates an extreme experimental situation where 99% of the diffracted intensity areas are not experimentally available but are measurable only around the Bragg peaks. The *a priori* information available is the HRTEM map at 190 pm resolution, shown in Fig. 2(*d*). This map provides the low-resolution starting phase set and the support as constraints in real space within the indetermination due to the border region $S_{\rm b}$. For an

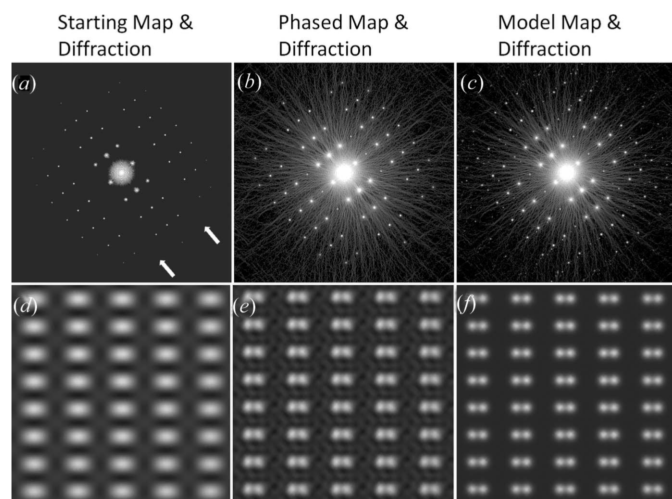

Figure 2
(a) Thresholded diffraction map, with only 1% of the higher moduli preserved. White arrows show rows of missing Bragg reflections cancelled out by the thresholding. (b) FT modulus of the phased map. (c) FT modulus of the model. (d) A zoom of a part – corresponding to the red square of Fig. 1(a) – of the low-resolution input map (representing the HRTEM map). (e) Zoom of the phased map in the region of the red square of Fig. 1(a). (f) Zoom of the model in the region of the red square of Fig. 1(a).

easier comparison, the magnified crystal projected potential of the model is reported in Fig. 2(f).

To verify if it is possible, starting from the information contained in Figs. 2(a) and 2(d), to retrieve the information of Figs. 2(c) and 2(f) through phase retrieval, we performed a series of tests.

First, we alternated $n_{\rm HIO}$ cycles of hybrid input–output (HIO) and $n_{\rm ER}$ cycles of error-reduction (ER) algorithms, with a period $T = n_{\rm HIO} + n_{\rm ER}$ (Fienup, 1982; Marchesini *et al.*, 2003; Marchesini, 2007), changing the number of the HIO and ER cycles and the feedback parameter value, starting both from random and low-resolution HRTEM phase sets. In fact, previous studies show that combination of HIO and ER is effective (even for reconstruction of a complex-valued object) (Fienup, 1987; Marchesini *et al.*, 2003; Huang *et al.*, 2007; De Caro *et al.*, 2010). But in our case this combined algorithm never converges to a satisfactory solution for any combination of HIO and ER cycles and feedback parameters, even using a perfect knowledge of the support ($S_{\rm b} = \{0\}$). Indeed, if most of the experimental intensities are unavailable, the algorithm does not converge to the solution when modulus and phase are simultaneously updated for the unobserved data (De Caro *et al.*, 2010). To overcome this inconvenience, the estimated moduli have to be kept fixed during several cycles in the same period T and only the corresponding phases have to change during the application of the fast Fourier transform (FFT), after support projection. Thus, unobserved moduli have to be updated every period T while the corresponding phases change every cycle (De Caro *et al.*, 2010).

Hence, we implemented a modified version of the phasing algorithm discussed in De Caro *et al.* (2010). The tested algorithm alternates $n_{\rm HIO}$ HIO cycles and $n_{\rm ER}$ of ER and the unobserved data were estimated periodically only at the ER cycles (De Caro *et al.*, 2010). Thus, they are kept fixed during the next $n_{\rm HIO}$ HIO cycles and re-estimated at the next ER cycles, and so on. Our tests have shown that periods T composed of several tens of $n_{\rm HIO}$ cycles and a few $n_{\rm ER}$ cycles are the best compromise to maximize convergence speed and quality of the phase-retrieved map. The support indetermination has been taken into account during phasing with an approach similar to that of Liu *et al.* (2012). Indeed, we have multiplied the phased map at the end of each iteration by $I - S_{\rm b}$, with I the identity matrix. This is equivalent to putting equal to zero the values of the phased map in $S_{\rm b}$ with a smooth edge border profile. The results of the algorithm obtained with $T = 20$ ($n_{\rm HIO} = 19$, $n_{\rm ER} = 1$) applied to the data in Figs. 2(a) and 2(d) are shown in Figs. 2(b) and 2(e). The reliability of the phased map can be estimated by comparing the results with the model diffraction and the map in Figs. 2(c) and 2(f), respectively. We caution the reader that the convergence is obtained only starting from the HRTEM phase set. When starting from a random phase set the algorithm does not converge. In fact, the use of low-resolution information in the starting cycles of the phasing process is fundamental in reaching a reliable solution (Huang *et al.*, 2009; De Caro *et al.*, 2010). For this reason in the first period T we have combined the phased map $V_j(r)$ obtained at the jth cycle with the starting map $V_0(r) = V_{\rm HRTEM}(r)$, *i.e.*

$$V_j(r) = [(T-j)V_{j-1}(r) + jV_{\rm HRTEM}(r)]/T. \qquad (1)$$

Moreover, the starting feedback parameter β has been chosen to be very low: $\beta = 0.1$. In this way all the unobserved moduli can be better estimated during the iterations of the first periods T, as the applied map modifications do not introduce strong perturbations. In this way all of them can be used in the phasing process and it is not necessary to select the stronger ones (De Caro *et al.*, 2010). We monitored the phasing process through some figure of merit, such as the error metric E, the R factor on the observed moduli ($R_{\rm obs}$) and on unobserved moduli ($R_{\rm unobs}$):

$$E = \left[\sum_{x\notin S} \left|V_j(r)\right|^2 / \sum_{x\in S} \left|V_j(r)\right|^2\right]^{1/2}, \qquad (2)$$

$$R_{\rm obs} = \sum_{k,{\rm obs}} \left|I_j(k)^{1/2} - I_{\rm obs}(k)^{1/2}\right| \Big/ \sum_k I_{\rm obs}(k)^{1/2}, \qquad (3)$$

$$R_{\rm unobs} = \sum_{k,{\rm unobs}} \left|I_j(k)^{1/2} - I_{\rm unobs}(k)^{1/2}\right| \Big/ \sum_k I_{\rm unobs}(k)^{1/2}. \qquad (4)$$

The latter, obviously, can be evaluated only for simulated data, but it is important to verify the efficiency of the algorithm to handle missing experimental information. Working on simulated data also, the correlation coefficient between the phased map and the model or the mean phase error can be evaluated to monitor the phasing process. Furthermore, when the error metric E becomes sufficiently low, less than a given threshold σ_1, this means that the unobserved moduli have been stabilized and one can allow their updating every cycle, even during the HIO cycles, instead of every period T. Finally, in order to

avoid eventual phase stagnation problems, when the error metric E becomes lower, below another suitable threshold σ_2, the HIO feedback parameter β can be put equal to one. We adopted this strategy to avoid the use of large β values at the beginning of the phasing process which lead to strong map perturbations and, consequently, to a worse estimation of the 99% of the unobserved weaker reflections.

The final correlation between the phased map and the model map, shown in Fig. 2, is about 98%, with a final mean phase error of about only 7° calculated on the 1% of the strongest moduli (the observed ones) and of about 16° on the remaining 99% weaker unobserved moduli. The two E threshold values have been set to $\sigma_1 = 0.003$ and $\sigma_2 = 0.0003$. Equivalently, one can obtain similar results with the following choices: (i) using low β values for a few hundred cycles and then allowing larger β values; (ii) updating the unobserved moduli estimated values every T cycles for the first one or two periods and then every cycle. The residual factor at convergence – after a few hundred cycles – calculated on the *unobserved* moduli is about $R_{\rm unobs} = 0.10$, whereas, at convergence, $R_{\rm obs}$ on the 1% of the stronger observed moduli goes down to 4×10^{-5}. The final E value is 3×10^{-5}. The possibility to verify, through simulated data, the efficiency of the phasing to recover the values of 99% missing in-between Bragg-diffracted (IBD) weak intensities with a very low final residual factor – only about 10% – and a very low final mean phase error – only 16° – constitutes an indirect proof that a reliable phase retrieval of KEDI data is possible. Indeed, by comparing Fig. 2(*b*) with Fig. 2(*c*) it is evident how the IBD scattering has been correctly retrieved. Only high-order diffraction peaks that were not already present in the input diffraction (Fig. 2*a*) are not retrieved. Also the satellite extra-Bragg peaks, which are visible in Fig. 2(*c*), are not present in the phased map. Let us note that these satellite peaks are related to very small non-periodicities due to the numerical approximation adopted to calculate the lattice period, when *real* coordinate values are approximated by a discrete matrix of integer numbers of pixels. The more evident differences between the phased and the model maps are the lower resolution of the former (larger atomic columns) and a non-uniform background in between atomic columns in Fig. 2(*e*), related to the *finite* (non-null) value of the final mean phase error reached through the phase retrieval. Fitting the projected atomic column peaks with Gaussian functions leads to a spatial resolution of the phased map of about 65 pm. This resolution, worse than that of the model (58 pm), is due to the diffraction pattern threshold, which cancels some high-resolution information. This lost high-resolution information cannot be completely restored through phase retrieval. Let us also note that there are two rows of missing Bragg reflections in the threshold input diffraction map (see the white arrows in Fig. 2*a*). Actually they are forbidden reflections for the Si ideal crystalline diamond structure. Nevertheless, they are very weak but still present in the FT of the model (Fig. 2*c*), missing in the thresholded input diffraction pattern (Fig. 2*a*) and partially retrieved through the phasing process (Fig. 2*b*). The use of a perfect support knowledge ($S_{\rm b} = \{0\}$) allows one only to obtain a slightly better estimate of moduli and phases of unobserved IBD: a lower final residual factor – about 8% – and a lower final mean phase error – about 12°. This proves that perfect knowledge of the border is not crucial for solving this KEDI phase problem. This can be justified by the quite negligible scattering power of the shell border region $S_{\rm b}$, the probe intensity being close to zero in that region. The ratio of the integral of the model map calculated inside the border shell region $S_{\rm b}$ with respect to the integral of the whole map is less than 2%. In other words, we approximate with zero an already weak scattering region (Liu *et al.*, 2012).

In the following test we considered an extreme case in which only the size and shape of the beam are available as *a priori* knowledge and no information on the projected potential is available within the HRTEM image (Fig. 3*a*). In this respect it should be noted that in a KEDI experiment it is not necessary to know/retrieve the incident wavefield phase. This finding can be demonstrated by applying the Van Cittern–Zernike theorem (Born & Wolf, 1991), the transmission electron microscope source being incoherent in nature (the spatial coherence is developed through wave propagation) and the diffraction pattern is measured in a far-field geometry (for details see Appendix *D*).

Fig. 3(*b*) shows the phased map obtained after 1000 cycles of our algorithm. The correlation coefficient values between the phased map and the model, as a function of the iteration number, are shown in Fig. 3(*c*). The obtained maximum value of about 95% is close to that (98%) obtained by starting the phasing from the HRTEM map in Fig. 2(*d*) (compare Fig. 3*b* with Fig. 2*e*). In Fig. 3(*d*) the behaviour of the object-domain error metric has been reported. Different regions of the phasing algorithm have been highlighted in correspondence with the changes of the IBD moduli update frequency and the β value. The effect of the ER cycles, at the end of some

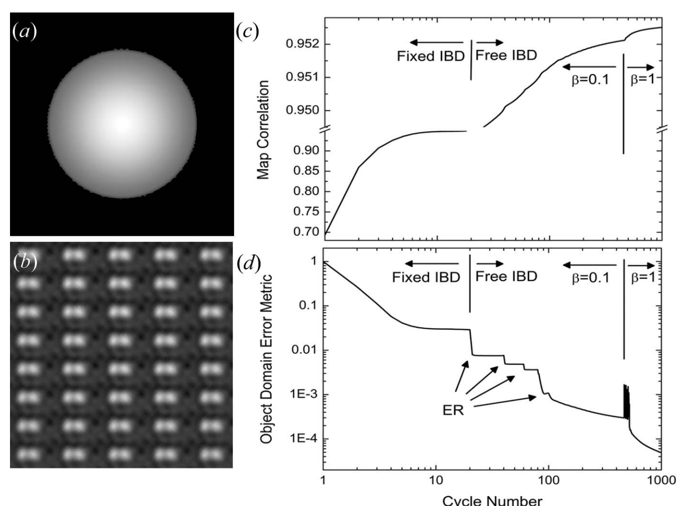

Figure 3
(*a*) Enlarged view of the incident beam probe. (*b*) Zoom of the phased map in the region of the red square of Fig. 1(*a*). (*c*) Correlation coefficient between the phased map and the model as a function of the cycle number. (*d*) Object domain error metric E as a function of the cycle number. IBD denotes the in-between Bragg diffraction unobserved intensities (see Appendix *A*).

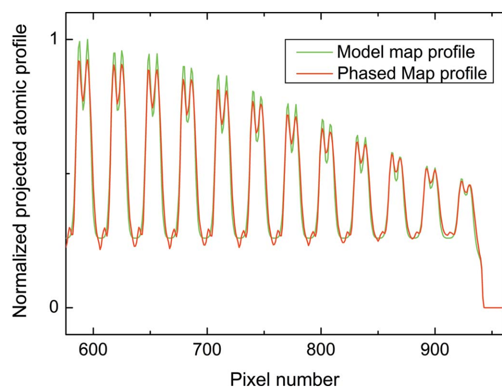

Figure 4
Profiles along the radius of the illuminated area in the [11$\bar{1}$] direction obtained after 1000 cycles starting the phasing from the initial map of Fig. 3(*a*) (only the beam probe and no HRTEM lattice fringes) and the map of Fig. 2(*a*) (the support and the projected Si potential at a resolution of 190 pm).

periods, is also shown. We have introduced a break in the plot of Fig. 3(*c*) to enlarge the scale when the algorithm uses free IBD. The aim of this is to show the small growths in correlation after several cycles. In fact, after a few tens of cycles the map correlation value is already close to its maximum value. After 1000 cycles we found $R_{\rm obs} \simeq 8 \times 10^{-5}$, $E \simeq 3 \times 10^{-5}$ and $R_{\rm unobs} \simeq 0.14$.

In Fig. 4 the intensity profiles between the phased (red curve) and model map (blue) are compared along a line in the [11$\bar{1}$] direction coincident with the radius of the illuminated area. The differences are essentially caused by a worse resolution due to the lack of high-index Miller reflections missing in the starting thresholded diffraction map (Fig. 2*a*). Only little artifacts on the minimum of the potentials can be noted (non-uniform background). These fluctuations are usually found in every phased map. In this case they could be ascribed to the lack of information due both to the 99% missing weak reflections and to the higher-index Miller reflections. Nevertheless, let us note that the function shown in Fig. 4 is not periodic, because the Si periodic projected potential has been integrated within a non-periodic beam probe. The possibility of correctly retrieving also the non-periodic part of the projected atomic potential of a crystalline nano-region – through phase retrieval of *incomplete* KEDI diffraction patterns (Fig. 2*a*), with many missing IBD intensities – is particularly interesting.

As a final remark let us note that by neglecting 99% of the IBD diffracted intensities and using an oversampling ratio S = 9.4 we are not in the theoretical conditions described in Appendices *A* and *B*. In fact, in an experimental situation with these values of missing IBD and oversampling ratio, the *measured* diffracted intensities would not be larger in number with respect to the unknown quantities, *i.e.* with respect to the projected potential intensities in the support and unknown phases. Nevertheless, the phasing could give a reliable phased map just because the missing information concerns the weaker reflections, close to zero. In other words, the *known* diffracted intensities given by the sum of the *measured* ones and the *correctly estimated* (the weaker ones approximated with zero) could be enough to solve the phase problem. Indeed, our tests indicate that an approximate estimation of these weaker IBD intensities is enough to permit the phasing algorithms to converge towards the right solution. This result is well known in other fields such as crystallography of proteins (Caliandro *et al.*, 2005). However, it is also important to underline that the $R_{\rm unobs} \simeq 0.14$, obtained starting with the beam probe map, is larger than the value $R_{\rm unobs} \simeq 0.10$ obtained starting with the synthetic HRTEM map. Indeed, we should not forget that we are dealing with an *extension* of phase information from low to high resolution, and the 99% of missing weaker IBD intensities and the non-perfect knowledge of the support border prevent one from performing any effective *ab initio* phasing, confirmed by the fact that when starting with random phases the algorithm does not converge towards a reliable solution.

3. KEDI experiments in a transmission electron microscope

The experiments were performed using a JEOL JEM 2010 F UHR operated at 200 kV. The cathode is a high-coherence Shottky type. The microscope has an objective lens with a low spherical aberration coefficient $C_{\rm s}$ = 0.47 (1) mm and a resolution at optimum defocus in HRTEM of 190 pm (Van Dyck, 1992). The environment around the microscope is thermally and mechanically very stable allowing one to achieve in the scanning annular dark-field mode (HAADF-STEM) the resolution of 126 pm theoretically expected for the electron optical setup used (Carlino & Grillo, 2006). In a KEDI experiment the experimental setup produces an electron nano-beam. The latter defines the mathematical support of the scattering function for the illuminated nanometric region of the extended crystal. As in a microscope the field of view is proportional to the inverse of the magnification, the size of the illumination function (beam size) is somehow related to the spatial resolution ρ. KEDI requires an HRTEM image and a nano-diffraction pattern acquired from the same sample area and using the same illumination condition. The electron beam size S (which defines the support) is directly related to the final resolution to be achieved and to the size of the detector used to record the HRTEM image and nano-electron diffraction (n-ED) pattern. In fact, if the highest frequency of the diffraction signal recorded in reciprocal space is $1/\rho$ pm^{-1}, we should have ρ at least two or three times the pixel size $\Delta_{\rm map}$ of the phased map to have an electron projected potential two-dimensional map calculated with a sufficient number of points to be plotted continuously. For example, if we could reach a final resolution – after the phase-retrieval process – of ρ = 70 pm we would have $\Delta_{\rm map} \sim$ 25–30 pm which, multiplied by the detector pixel number along a line, N = 1024 in our experimental case, would lead to a spatial region O (scattering region plus non-illuminated surrounding region) of 25–30 nm in size. Moreover, for the Nyquist theorem's requirement, the illuminated beam size S (the support) has to be less than $1/(2^{1/2})O$, *i.e.* at a maximum of ~17–20 nm in size. Hence, in order to properly run the phase-retrieval algorithms, the

illuminated region of the sample in the direct HRTEM image has to be properly chosen with respect to the whole detector area to satisfy the above KEDI oversampling condition.

Here, experimentally the cathode emission condition and the electron optical illumination system of the microscope have been set up to increase the probe coherence on the smallest illuminated area achievable. There is an intrinsic benefit of a KEDI experiment: no substrate/film/membrane is needed to hold the sample, as happens for normal EDI (Zuo *et al.*, 2003; Huang *et al.*, 2009; De Caro *et al.*, 2010) realized on isolated nano-crystals, avoiding any problem related to parasitic background scattering, and thus increasing the signal-to-noise ratio of the measured diffraction data. Furthermore, the electron optical conditions used allow recording of an n-ED pattern without the need for the beam stopper and hence all the diffraction intensities are available for the phasing. The microscope has an illumination system composed of three magneto-static lenses. These lenses were operated independently, together with the electrostatic lens of the emitter, to produce the smallest probe on the focal plane of the pre-field of the objective lens and hence the smallest coherent parallel beam on the specimen. The emission conditions of the microscope cathode were chosen to increase the coherence of the electron probe by decreasing the temperature of the emitting tip. We used a heating current for the filament that halves the emission current with respect to the standard operation, decreasing at the same time the electron dose delivered to the specimen. This configuration together with a condenser aperture of 10 µm in diameter allowed us to obtain a confined beam of a minimum diameter between between 5 and 10 nm at the sample position and hence well satisfying the sampling requirement for the phase-retrieval process. The current density on the specimen was below the detection limit of the amperometer connected to the phosphorus screen of the microscope (<0.1 pA cm^{-2}), allowing us to acquire the relevant diffraction pattern on the 1024 × 1024 charge-coupled device (CCD) camera without using the beam stopper for the direct beam. Thus all the diffracted intensities were available for the phasing process and a very small dose is delivered to the specimen. The small electron probe without any changes was used to acquire both the HRTEM image and diffraction from the same area of the specimen. As a case study, the KEDI proof of concept was carried out on a silicon crystal cross section prepared in ⟨112⟩ geometry, a benchmark for resolution, by mechanical grinding, polishing and final ion-beam milling (Carlino, 2008).

Figs. 5(*a*) and 5(*b*) show the square root of the measured n-ED patterns from 6 and 12 nm-thick sample regions, respectively. These thickness values were chosen to elucidate the role of the dynamical diffractions on the method. The n-ED patterns have been thresholded to 5% of the maximum intensity for a better display of the weak reflections. Red arrows highlight the same forbidden reflections for the Si crystal, mostly due to dynamical effects.

White arrows point to the highest-order Miller-index reflections, with the corresponding lattice spacing down to 71 pm and hence more than enough to solve the Si dumbbell spacing in the [112] projection of 78 pm. In Fig. 5(*c*) a scan of the n-ED patterns along the $[11\bar{1}]$ crystallographic direction is reported. The comparison shows that the n-ED pattern of the 6 nm-thick sample region is, to a good approximation, kinematical, the amplitude of the forbidden reflection $(\bar{2}\bar{2}2)$ being about 4% of the $(\bar{1}\bar{1}1)$. Conversely, the dynamical effects for the n-ED pattern of a 12 nm-thick sample region are much stronger, the amplitude of the forbidden $(\bar{2}\bar{2}2)$ reflection being about 30% of the relevant $(\bar{1}\bar{1}1)$. The measurements are in agreement with the simulated full dynamical calculations performed by *JEMS* (http://cimewww.epfl.ch/people/stadelmann/jemsWebSite/jems.html) for a specimen slightly tilted by about 0.2°. We caution the reader that the two n-ED patterns have been differently scaled in the abscissa axis in order to better visualize their differences.

In order to show a proof of concept for KEDI, we have combined the modulus of the HRTEM image FT with the measured n-ED pattern peaks. In fact, the n-ED pattern has been suitably thresholded close to the reciprocal-lattice nodes in a circular region of 5 pixels in radius, to select just the higher-intensity values around each diffraction maximum. The KEDI diffraction pattern used for the phasing has been obtained by selecting these regions around the Bragg peaks of the diffraction experimental pattern and combining them with the modulus of the HRTEM image FT, following the matching procedure described elsewhere, requiring rotation and scaling of the HRTEM FT (Huang *et al.*, 2009; De Caro *et al.*, 2010). The pattern has been centrosymmetrized because the imaginary part is correlated only to the tilt angle and

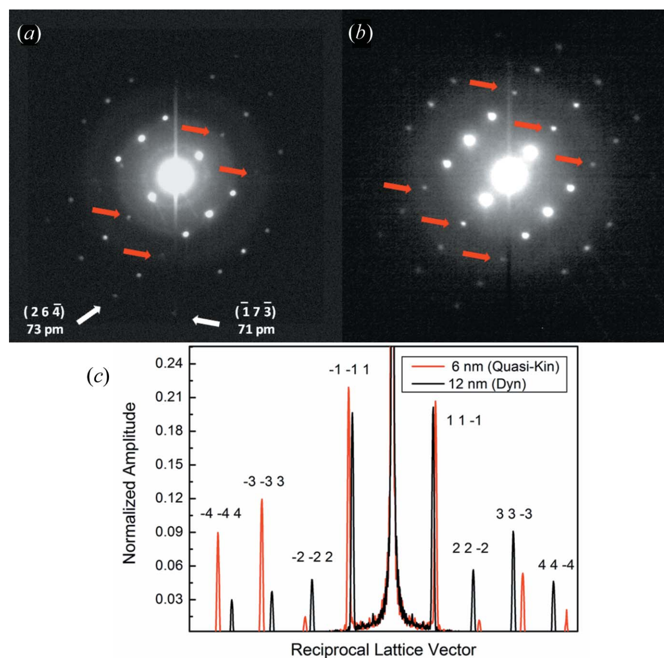

Figure 5
Keyhole n-ED of an Si crystal in the ⟨112⟩ zone axis. (*a*) Square root of the measured n-ED pattern of a 6 nm-thick sample region; (*b*) square root of the measured n-ED pattern of a 12 nm-thick sample region. Red arrows point to the same forbidden reflections for the Si crystal. (*c*) Scans of the n-ED patterns of (*a*) (red curve) and (*b*) (black curve) along the $[11\bar{1}]$ crystallographic direction. The two patterns have been differently scaled in the abscissa axis to better visualize their differences.

absorption and does not contain any further information about the unknown projected atomic potential (see Appendix *C*). An alternative procedure is that used by Huang *et al.* (2009) or De Caro *et al.* (2010), by imposing at the beginning of the phase process the real constraint and removing it after some iterations to allow the small imaginary part of the object scattering function to be different from zero. Thus we obtained an experimental pattern with characteristics similar to those used in the simulations, with only the stronger diffraction intensity values used in the phasing process, and approximating with zero the IBD intensities when they are below a given threshold. The resulting diffraction pattern is shown in Fig. 6(*a*) and is characterized by having only about 5% of intensities different from zero. Let us remember that in the simulated tests of the previous section we left less than 1% of the intensities different from zero. Nevertheless, the phases have been correctly retrieved. Thus, we merged (Huang *et al.*, 2009; De Caro *et al.*, 2010) the n-ED pattern with the low-frequency information, computed from the HRTEM FT, to correctly transfer into the Fourier space the finite support information of the scattering function (see Fig. 6*a*).

Fig. 6(*b*) shows the raw low-magnification HRTEM image (*S*) as acquired on a 6 nm-thick sample region. The specimen is illuminated by a 6 nm-diameter electron beam (*S*), which gives an oversampling ratio of about 20, if compared with the detector area (*O*), 25 nm in linear size. To optimize the display of Fig. 6, we show a rectangular area of the whole originally square HRTEM image, cutting, in the composition of the figure, two black strips either side of the illuminated region. Although the size of the incident beam is so small (6 nm), a relatively large number of Si-crystal in-plane unit cells – $n_{\rm cell} \sim \pi[(S/2)/d_{\rm cell}]^2$ – contribute to the diffraction process. In the case under study, taking into account the [112] zone-axis orientation of the Si crystal in the calculation of the unit-cell size $d_{\rm cell}$, it results in $n_{\rm cell} \sim 100$. This leads to a diffraction pattern well confined around the reciprocal-lattice nodes, giving an extremely small diffracted intensity almost everywhere in between Bragg peaks.

Fig. 6(*c*) is the two-dimensional projected Si-crystal potential image obtained by applying the algorithm discussed in the previous section on the diffraction data of Fig. 6(*a*), multiplied by the illumination function, namely the beam profile. Fig. 6(*d*) is a zoom of the central part of Fig. 6(*c*) in which the Si dumbbells in the [112] zone axis, spaced by 78 pm, can be clearly distinguished in the phased map. The spatial resolution of this map can be estimated by the FWHM of the Gaussian functions fitting the projected atomic column peaks. The obtained result is about 71 pm. Let us observe that the dumbbells were not resolved in the original HRTEM image because of the lens-aberration-limited resolution of about 190 pm at the optimum defocus. Fig. 6(*e*) shows the phased image for a 12 nm-thick specimen region, where strong dynamical effects are present (see Fig. 5*b*).

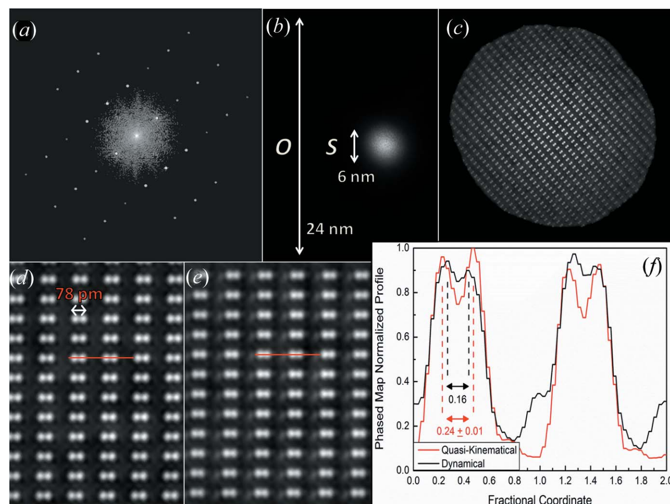

Figure 6
Keyhole EDI of an Si crystal in the ⟨112⟩ zone axis. (*a*) KEDI diffraction pattern, utilized for the phase retrieval, for the 6 nm-thick sample region. (*b*) Low-magnification HRTEM image (*S*) in the 6 nm-sized illuminated area (magnifying the image the relevant lattice fringes will be displayed), compared with the whole detector area (*O*), which is about 25 nm in size. (*c*) Two-dimensional projected Si-crystal potential phased image for the 6 nm-thick sample region. (*d*) Zoom of the central part of (*c*) in which the two sublattices of the diamond Si crystal structure are resolved. (*e*) The equivalent of (*d*) obtained by the phase retrieval of KEDI data for the 12 nm-thick sample region. (*f*) Comparison between the scan along the lines of (*d*) and (*e*). The closest projected atomic columns in the phased map of the 6 nm-thick sample region are correctly spaced (see red curve) compared to the nominal value of 0.25, whereas in the 12 nm-thick sample region they are wrongy spaced (see black curve).

4. Discussion of experimental results

The comparison between the phased images corresponding to sample regions of different thickness points out the role of the dynamical diffraction effects in the image reconstruction. This is highlighted in Fig. 6(*f*) with the comparison between the scan along the lines of Figs. 6(*d*) and 6(*e*). The line profile shows that the closest projected atomic columns in the phased map of the 6 nm-thick sample region are correctly spaced (see the red curve), *i.e.* 0.25 in fractional coordinates, as expected for the Si structure. Conversely, the closest projected atomic columns in the phased map of the 12 nm-thick sample region are wrongly spaced (see the black curve). In the latter, their distance is only 0.16 in fractional coordinates, corresponding to an unphysical distortion of the Si structure, which leads to a reduction of $0.25 - 0.16 = 0.09$ in fractional coordinates of the closest projected atomic columns. In turn, this would correspond to an unphysical distance of only about 72 pm of the two diamond sublattices in the [112] zone-axis projection. Let us also note that in the presence of strong dynamical effects, the real-object constraint would also cause inaccurate reconstructions in the phased maps (Huang *et al.*, 2007). Conversely, the possibility of correctly retrieving the average projected Si crystal structure in a [112] zone-axis orientation with a KEDI experiment, even in the presence of a small dynamical effect (see Figs. 6*d* and 6*f*), is very interesting because it indicates that the methodology can also work with non-perfectly kinematical diffraction patterns, which in electron microscopy are actually an idealization. Indeed, it is already known that the Fourier components with the smallest amplitudes are not very

important for solving a structure as long as the phases of the larger amplitudes are correctly retrieved (Zuo, 1995, p. 94). Moreover, a potential map is practically unaffected even when deleting the weaker reflections if those corresponding to the highest spatial resolution are preserved (Zuo, 1995, p. 94). This explains why the periodic projected electrostatic potential was correctly found even if only the n-ED pattern highest-intensity values around each diffraction maximum were used for phasing, but correctly constrained through the low-angle scattered amplitude obtained by the HRTEM image FT. This agrees with the theoretical simulations of the previous paragraph, where 99% of weaker FT components have been approximated with zeros and, nevertheless, the original potential has been correctly retrieved by phasing the relevant approximated KEDI pattern. Furthermore, this finding explains why the EDI/KEDI approach can tolerate, up to a certain degree, the presence of dynamical effects in the diffraction pattern. In fact, it can be shown that weaker reflections are just those that suffer the larger *relative* variation in amplitude due to multiple scattering, *i.e.* the larger $[I(\mathbf{k})_{\rm dyn} - I(\mathbf{k})_{\rm kin}]/I(\mathbf{k})_{\rm kin}$ (Zuo, 1995, p. 21). For a quasi-kinematical forbidden reflection, such as the $(22\bar{2})$ reflection for an Si crystal, this relative variation in amplitude is of course very high. Nevertheless, if this variation, due to the dynamical effects, leaves the reflection always weaker than dominant ones, the projected potential can be correctly retrieved (see Figs. 6*d* and 6*f*). Conversely, if the dynamical effects are so strong as to cause the change of a weak forbidden reflection into a dominant one, the projected potential cannot be correctly retrieved (see Figs. 6*e* and 6*f*), producing image artifacts.

Another striking result of the proposed KEDI approach is the evidence of in-plane strain in the phased maps of the nano-beam illuminated regions. In fact, the stress, due to the amorphous layers always formed on the sample free surfaces during the ion-beam milling process necessary to prepare the thin specimen for TEM experiments, induces a lattice relaxation in the thinner areas of the silicon cross section (Banhart, 1994). In fact, both Figs. 6(*d*) and 6(*e*) show oblique non-perfectly rectangular in-plane projected unit cells as evident also in a careful analysis of the n-ED pattern geometrical distortion. However, the in-plane strain changes as a function of the region thickness (Banhart, 1994). It is $8 \times 10^{-3} \pm 1 \times 10^{-3}$ in the 12 nm-thick sample region (Fig. 6*e*) and $11 \times 10^{-3} \pm 1 \times 10^{-3}$ in the 6 nm-thick sample region (Fig. 6*d*). This finding confirms the potentialities of the KEDI approach to image at sub-ångström resolution subtle details of the structural properties of extended crystals on an illuminated area of 5–10 nm.

5. Conclusions

We studied the peculiarities of the EDI/KEDI phase problem showing how the *a priori* knowledge of the support and low-resolution phases, obtained by the relevant HRTEM image, produces enough information to recover the phase information lost in acquiring the EDI/KEDI electron diffraction pattern. We presented a general electron diffractive imaging approach suitable to study extended crystals, overcoming previous restrictions to isolated nano-objects. These findings demonstrate how sampling requirements for phase retrieval can be satisfied by properly limiting the size of the coherent electron plane wave illuminating the extended object. The nano-electron diffractions, obtained by using the experimental setup described here, satisfy the sampling requirement to derive the relevant phases. We have shown that KEDI is also relatively robust with respect to the dynamical interactions between the excited Bloch waves within the crystal, up to a certain threshold where artifacts in the phased image appear. In this respect it should also be noted that – to avoid artifacts – supports with very sharp profiles (top-hat functions) are mandatory only to solve the phase problem involving complex scattering functions. In fact in this case one is dealing with two phases to be retrieved: a complex function in real space (the scattering function) and another in Fourier space (related to its Fourier transform). In the case of EDI/KEDI we have shown that the imaginary part of the potential does not contain further structural information with respect to the real part. For this reason the first step in the EDI/KEDI phasing process can be achieved also by imposing that the unknown function (potential) is real. This is equivalent to supposing a centrosymmetrical diffraction pattern and this does not introduce any artifact because the imaginary part is proportional to the real part. The small imaginary part can be retrieved by relaxing the real constraint after the reconstruction of the real scattering potential. The simulations have shown that, even working with real functions, a truly *ab initio* phasing is very difficult to achieve, due to the experimental lack of the weakest intensities in between Bragg peaks. Knowledge of the incident beam shape and profile is, however, sufficient to overcome this limit.

The method allows one to obtain currently, by using standard microscopes, spatial resolution comparable with that achieved with spherical-aberration-corrected equipment, allowing the study of extended material systems at higher resolution and accuracy. In a forthcoming paper we will discuss the application of KEDI to the study of crystalline defects.

APPENDIX *A*
The problem of the missing diffraction data in between Bragg peaks for EDI/KEDI experiments

In 1999 a breakthrough was achieved by Miao *et al.* (1999), who showed experimentally that when the object is finite in size, the relevant diffraction pattern can be oversampled beyond the Nyquist frequency to get twice the number of data, sufficient to recover both amplitude and phase. The theoretical premises of this work were already present in Sayre's paper (Sayre, 1952*a*), based on Shannon's sampling theorem (SST) (Shannon, 1949), about the effect of a finer-than-crystallographic sampling of a diffraction pattern. In crystallography, in-between Bragg-diffracted (IBD) intensities are

not measured. Also for nano-crystals IBD intensities are not experimentally accessible or they are buried in the background. In fact, the size of the incident beam for KEDI or the size of the nano-crystal for EDI, even if ranging on the scale of 5–10 nm, is much larger than the crystalline unit-cell size. In turn, this causes the intensity between the neighbouring reflections to be only two or three orders of magnitude less than the Bragg intensities, often too close to the noise level to be registered with a large enough signal-to-noise ratio. For instance, it would be easy to verify that, if the shape function defining the incident beam is Gaussian with a width of n unit cells, its FT will also be Gaussian with a width of about $1/n$ the distance between the Bragg spots, so that halfway its intensity would usually be negligible.

Hence, the phase problem seems to be particularly ill-posed for two-dimensional diffraction patterns for EDI or KEDI, because the interferences of the many unit cells yield relatively strong diffraction spots close to the reciprocal-lattice nodes of the corresponding crystal, and a very weak diffracted signal elsewhere in reciprocal space. Thus, in principle, both for the crystallographic and the EDI phase problems, theoretical considerations about the uniqueness of the phase solution, derived by the SST, are not strictly applicable. Nevertheless, the great success of crystallography in solving crystal structures shows that mathematically ill-posed problems can have a unique phase solution provided that robust phasing approaches are used. In fact, the lack of IBD intensities is compensated for by other *a priori* information about the unknown scattering function. For example, in crystallography, for the electron-density function, this further *a priori* information can be its positivity and atomicity (Sayre, 1952*b*). Also the diffraction patterns obtained by EDI/KEDI experiments may not contain enough information to be used in a reliable and unique phase-retrieval process, if any further *a priori* information is not available. This particular situation of a diffraction pattern, which is partially like that of a crystal and partially like that of a non-periodic object, will be denoted as the EDI/KEDI phase problem.

In the case of a positive real and non-periodic image, uniqueness of the phase problem in two dimensions was shown by Bates (1982, 1984) using just arguments from the sampling theory. Walther (1963) demonstrated that in the one-dimensional case there are multiple, but countable, phase functions that lead to images with the correct support. On the contrary, in two dimensions the solution is 'almost' always unique, because absolute position, inversion in the origin or constant phase factors are irretrievably lost – although they are usually of little practical significance – and 'pathological' structures such as the homometric ones are very rare (Hosemann & Bagchi, 1953). Uniqueness for general complex two-dimensional images was shown by Barakat & Newsam (1984). Moreover, in going from the one-dimensional to the two-dimensional case or to the N-dimensional case, by using a sample spacing twice the Nyquist spacing for each dimension (Bates' criterion), the phase problem goes from being non-unique to unique or to overdetermined (Millane, 1996; Miao *et al.*, 1998). Indeed, according to both numerical simulations and experimental results, Bates' criterion is overly restrictive (Miao *et al.*, 1998, 2003, 2008). All the above results are generally valid if the whole diffraction pattern is available. But what happens for an EDI/KEDI experiment for which large regions of the diffraction pattern – in between Bragg peaks – cannot be accurately measured?

To answer this question let us start to briefly revisit some well known fundamental concepts about the SST. When the SST is applied to the FT of a one-dimensional non-periodic object with scattering function $\rho(x)$ and spatial extents d, it follows that if the FT is known only at the points (h/d), then it is everywhere determined by the relation

$$F(u) = \sum_h F\left(\frac{h}{d}\right) \frac{\sin[\pi d(u - h/d)]}{\pi d(u - h/d)}. \qquad (5)$$

Thus, the magnitude and phase knowledge of all significant values of $F(u)$ at the Nyquist rate $(1/d)$ are enough to construct the image by using either a series expansion of $\rho(x)$ or, equivalently, using its continuous FT by means of the sampling theorem [equation (5)]. Unfortunately, phases are experimentally lost. Therefore equation (5) cannot be directly applied.

Therefore, when no other *a priori* information than the object support is available, the phase information can be recovered only by sampling the object diffraction pattern at a rate higher than the $F(u)$ Nyquist rate. This implies that samples of values of $|F(u)|$ must be obtained at points that are in between the conventional Bragg samples, corresponding to the $F(u)$ Nyquist rate that would be obtained by a periodic repetition of the same unit (the non-periodic scattering function) in space with period d. In other words, let us imagine repeating periodically the object scattering function of extension d everywhere in the space, like a crystal whose unit cell is just the object scattering function. The Bragg sampling corresponding to the Nyquist rate $1/d$ is not enough to solve the phase problem. A rate $1/2d$ is needed. This is often denoted by the term oversampling if referred to the $F(u)$ Nyquist rate, but it is just the Nyquist sampling needed to satisfy the sampling theorem for the diffracted intensities $I(u)$. In fact, as the spatial extent of the autocorrelation function, $A(r) = \mathrm{FT}^{-1}[I(u)]$, is twice that of the object scattering function in each direction, applying the SST at the measured intensity $I(u) = |F(u)|^2$ yields

$$I(u) = F(u)F^*(u) = \sum_h I\left(\frac{h}{2d}\right) \frac{\sin[2\pi d(u - h/2d)]}{2\pi d(u - h/2d)}, \qquad (6)$$

where the * indicates the complex conjugate. Even if equations (5) and (6) can be generalized to more than one dimension, a one-dimensional formalism will be used here to simplify the formalism. The sampling condition in equation (6) would lead to an overdetermination for phase problems in more than two spatial dimensions (Miao *et al.*, 1998).

As previously discussed from an experimental point of view, the correct sampling of the modulus of the FT of the object scattering function can be realized with: (i) coherent plane waves illuminating a region suitably larger than an isolated

object scattering function, with an empty region around it, or (ii) by using a finite illuminating function to study extended (non-isolated) scattering objects. This is equivalent to defining a new unit cell of size $2d$, with the object scattering function occupying only half of it. The 'virtual periodic structure' obtained by the periodic repetition of this new bigger unit cell would make accessible, from an experimental point of view, all reflections $I(h/2d)$ needed to apply equation (6) and to find a unique solution to the phase problem (Bates, 1982, 1984; Barakat & Newsam, 1984).

In order to deal with the EDI/KEDI phase problem, let us start to consider the nano-crystal/illuminated nano-region scattering function as a whole single non-periodic object. The Nyquist sampling to be considered is $1/Md$ with M the number of unit cells inside the nano-crystal/illuminated nano-region and d the crystal unit-cell size. Let us note that this Nyquist sampling is much finer than the unit-cell Nyquist sampling $1/d$, at which Bragg diffractions occurs, corresponding to the periodic crystal atomic structure. In order to satisfy the oversampling condition for the nano-crystal/illuminated nano-region as a whole, since its autocorrelation function has an extension of $2Md$, the IBD intensities are those in correspondence with the Fourier space sampling points $n/2Md$, with n an odd integer. Between two consecutive Bragg spots of the unit-cell Nyquist sampling ($1/d$), we should measure $2M$ diffracted intensity values corresponding to the nano-crystal/illuminated nano-region as a whole, measured with the right sampling step $1/2Md$ and, consequently, satisfying the SST, as shown schematically in Fig. 7. For even *integers* $n = 2n'$ we would have $2n'/2Md = n'/Md$, *i.e.* the equivalent 'Bragg diffractions' corresponding to a supercell with size Md whose content is the entire nano-crystal/illuminated nano-region. The oversampling condition, satisfied for the supercell, would in principle allow one to also obtain IBD intensities when $n = 2n' + 1$ is odd. In fact, we should expect to have several of these $(2n' + 1)/2Md$ IBD intensities different from zero, but many others should be very close to zero (see Fig. 7).

In real experiments, the presence of noise, a low dynamical range of the detector or an excessively large number M of unit cells would cause many of the $2M$ nano-crystal/illuminated nano-region supercell scattered intensities at a sampling frequency $1/2Md$, in between two consecutive crystal unit-cell Bragg peaks, *e.g.* in between the k/d and the $(k + 1)/d$ unit-cell reciprocal-lattice nodes, to be too low to be detected. This loss of information should not be confused with the loss of information due to undersampling. Indeed, in the presence of undersampling very intense diffracted intensities could be lost due to the insufficient sampling $1/d$ of the diffracted intensity function whose Nyquist sampling is $1/2d$. Instead, by considering the nano-crystal/illuminated nano-region as a whole its diffraction pattern can be correctly sampled at the rate $1/2Md$ corresponding to half the Nyquist rate of an object scattering function with size Md. Therefore none of the intense diffracted intensities is lost. Only the weaker diffracted intensities below the noise level could be lost. But this is true for every diffraction pattern. It is worthwhile to remark that the approximation $I(u) = 0$ for an unobserved intensity, very close to zero, is already a good experimental approximation: we are approximating with zero diffracted intensities which are very weak, close to zero.

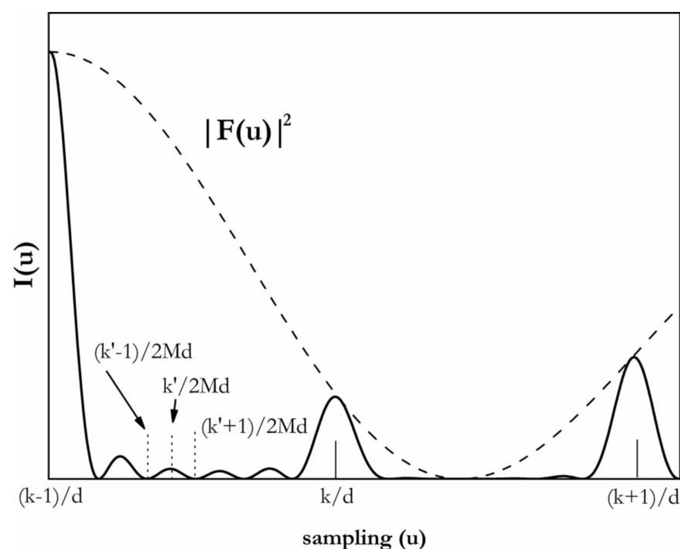

Figure 7
The difference between the unit-cell and the nano-crystal/illuminated nano-region Nyquist samplings is schematically shown. Nyquist sampling ($1/2Md$), corresponding with the nano-crystal/illuminated nano-region considered as a whole, is much finer than the $1/d$ unit-cell sampling. Here $F(u)$ is the FT of the unit-cell content and $I(u)$ is the scattered intensity obtained by the M unit cells.

Some of these weak intensities could be partially restored during the phasing process, as discussed by De Caro *et al.* (2010). In that work it was shown that the *partial* reconstruction of these weak intensities is useful to help the phase-retrieval process, as it is well known that phase information is much more important than intensity information. Indeed, for the weak experimentally lost diffracted intensities also an approximate knowledge is sufficient for reliable phase reconstructions. In other words, the nano-crystal/illuminated nano-region diffraction pattern could contain enough information to solve the phase problem. In the next appendix, we will further clarify this important point with the help of the generalized sampling theorem (GST) (Papoulis, 1977).

APPENDIX *B*
The generalized sampling theorem applied to the EDI/KEDI phase problem

We have already underlined that the FT of the nano-crystal/illuminated nano-region is a peaked function with some secondary maxima close to the main maximum (*e.g.* see Huang *et al.*, 2009). Usually, from an experimental point of view, only a few secondary maxima are intense enough to be measured beyond the noise background. The lack of a part of the diffracted intensities poses an important question. Is the diffraction information – experimentally available in EDI/KEDI experiments – enough to solve the phase problem? To clarify this point we will start from the results of the GST.

For the convenience of the reader, we first will revisit the main results of the GST. We will consider a one-dimensional

function $g(u)$ with spatial extent D. In order to explain the GST in simple words we could say that if we know not only the function $g(u)$ but also the sampled values of its derivatives or other linear functionals, the sampling interval can be increased. If we know N functionals of the function $g(u)$ to be calculated continuously, the sampling rate can be $(1/N)$th of the Nyquist rate $1/D$, with N the number of all functionals, including $g(u)$ (Papoulis, 1977, 1986). The function $g(u)$ can be calculated continuously for every u by means of the interpolation formula

$$g(u) = \sum_n \left\{ \sum_{j=1}^{N} a_{nj}\left[\pi D\left(u - n\overline{T}\right)\right] g_j\left(n\overline{T}\right) \right\}. \tag{7}$$

Here,

$$\overline{T} = NT = \frac{N}{D}, \tag{8}$$

$[g_1(n\overline{T}), g_2(n\overline{T}), \ldots, g_m(n\overline{T})]$ are the N functionals of $g(u)$ calculated at the sampling points $n\overline{T}$, with n an integer, *i.e.* at $(1/N)$th the Nyquist rate, and the interpolation functions are found by

$$a_{nj}(u) = \frac{1}{c} \int\limits_{-D}^{-D+c} \Phi_j(x, u) \exp(-in\overline{T}x)\, \mathrm{d}x \tag{9}$$

with $c = 2\pi/\overline{T}$, $a_{nj}(u) = a_{oj}(u - n\overline{T})$ and the $\Phi_j(x,u)$'s solutions of the set of equations

$$\left\{ \begin{matrix} H_1(x) & H_2(x) & \cdots & H_N(x) \\ H_1(x+c) & H_2(x+c) & \cdots & H_N(x+c) \\ \vdots & \vdots & & \vdots \\ H_1[x+(N-1)c] & H_2[x+(N-1)c] & \cdots & H_N[x+(N-1)c] \end{matrix} \right\} \times \begin{bmatrix} \Phi_1(x,u) \\ \Phi_2(x,u) \\ \vdots \\ \Phi_N(x,u) \end{bmatrix} = \begin{pmatrix} 1 \\ \exp[i(x+c)u] \\ \vdots \\ \exp\{i[x+(N-1)c]u\} \end{pmatrix}, \tag{10}$$

u is arbitrary and $-D < x < -D + c$. Clearly there is no solution if the above H matrix is zero (Papoulis, 1977, 1986).

Let us now see what the GST yields for bunched samples. In the case of a recurrent non-uniform sampling, as shown in Fig. 8, if the function f is known at the points $\alpha_j + n\overline{T}$ for $j = 1, \ldots, N$ and $\overline{T} = NT$, then it can be determined for any u (Papoulis, 1986; Marks, 1991) through the following interpolation equation:

$$g(u) = \sum_n \left\{ \sum_{p=1}^{N} g\left(n\overline{T} + \alpha_p\right) \sin c\left[\frac{\pi}{\overline{T}}\left(u - n\overline{T} - \alpha_p\right)\right] \times \prod_{\substack{q=1 \\ q\neq p}}^{N} \frac{\sin\left[(\pi/\overline{T})\left(u - n\overline{T} - \alpha_q\right)\right]}{\sin\left[(\pi/\overline{T})\left(\alpha_p - \alpha_q\right)\right]} \right\}. \tag{11}$$

N are the distinct locations where the irregular samples are measured inside a Nyquist interval. The function $g(u)$ is known at these irregular samples every N Nyquist intervals

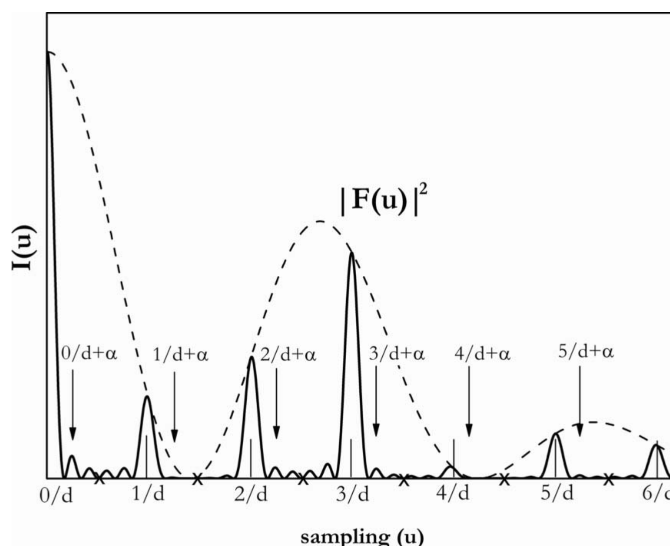

Figure 8
Example of bunched sampling, if $N = 2M$ and the function is the diffracted intensity I with $T = 1/2MD$, where M is the number of unit cells constituting the nano-crystal/illuminated nano-region. For simplicity only two interlaced samplings ($\alpha_1 = 0$ and $\alpha_2 = \alpha$) are shown. But the GST would require $N = 2M$ interlaced sampling, corresponding to different α_j values, with $j = 1, \ldots, N$.

and, for this reason, the bunched sampling is also denoted as an *interlaced* one (Marks, 1991).

Let us now consider a simple example. If $N = 2$ and the function to be interpolated is the diffracted intensity I by a crystal with $T = 1/2D$, $\alpha_1 = 0$ and $\alpha_2 = \alpha$, the GST [equation (11)] yields

$$I(u) = \frac{\cos[2\pi D(\alpha/2 - u)] - \cos(\pi D\alpha)}{2\pi D \sin(\pi D\alpha)} \times \sum_n \left\{ \frac{I(n/D)}{[u - (n/D)]} - \frac{I[(n/D) + \alpha]}{[u - (n/D) - \alpha]} \right\}. \tag{12}$$

In terms of the interpolation theory, equation (12) means that we know the samples every two Nyquist intervals $2T = 1/D$, in two points of these intervals, *i.e.* at n/D and $n/D + \alpha$. For example, if $\alpha = 1/2D$ and observing that $\overline{T} = 2T = 1/D$, equation (12) can be written as

$$I(u) = \frac{\sin(2\pi Du)}{2\pi D} \sum_n \left\{ \frac{I(2nT)}{(u - 2nT)} - \frac{I[(2n+1)T]}{[u - (2n+1)T]} \right\}. \tag{13}$$

As the first sum is over even values and the second over odd ones, equation (13) is just the SST formula ($T = 1/2D$)

$$\begin{aligned} I(u) &= \sum_n I(nT) \frac{\sin[2\pi D(u - nT)]}{2\pi D(u - nT)} \\ &= \sum_{\text{even}} I(2nT) \frac{\sin[2\pi D(u - 2nT)]}{2\pi D(u - 2nT)} \\ &\quad + \sum_{\text{odd}} I[(2n+1)T] \frac{\sin\{2\pi D[u - (2n+1)T]\}}{2\pi D[u - (2n+1)T]} \\ &= \frac{\sin(2\pi Du)}{2\pi D} \sum_n \left\{ \frac{I(2nT)}{(u - 2nT)} - \frac{I[(2n+1)T]}{[u - (2n+1)T]} \right\}. \end{aligned} \tag{14}$$

Equation (14) has been obtained by using the well known trigonometric function properties: $\sin(\alpha \pm \beta) = \sin\alpha\cos\beta \pm \cos\alpha\sin\beta$; $\cos(n\pi) = \pm 1$, with the upper (lower) sign holding for even (odd) integer n; $\sin(n\pi) = 0$ for any integer n. Let us note that when $\alpha = 1/2D$, we obtain that the irregular bunched samples $\alpha_1 = 0$ and $\alpha_2 = \alpha = 1/2D$ become regular, characterized by just the Nyquist sampling interval between all sampled data: the (twice) bunched sampling every two Nyquist intervals coincides with a single sampling in each Nyquist interval. This finding explains the result shown in equation (14).

Thus, the GST allows us to derive suitable interpolation formulae to reconstruct everywhere continuously a function by using bunched irregular samples instead of the usual regular Nyquist sampling. For the EDI/KEDI phase problem, if it is possible to individuate α_j points, with $j = 1, \ldots, N$, in Fourier space between two consecutive unit-cell Bragg spots, where the FT of the nano-crystal/illuminated nano-region still has a measurable intensity above the noise level, the phase problem could still have a reliable solution even if the whole diffraction pattern is not experimentally measured. Indeed, in the case of a recurrent non-uniform sampling, if the scattering function is known at the points $\alpha_j + n\overline{T}$ for $j = 1, \ldots, N$ and $\overline{T} = NT$, then it can be determined for any u (Papoulis, 1986; Marks, 1991) through the GST interpolation equation [equation (13)] for $g(u) = I(u)$.

In equation (13) N are the distinct locations where the irregular samples are measured within a Nyquist interval. The diffracted intensity function $I(u)$ is known at these irregular samples every N Nyquist intervals. If the measured intensity is obtained by the scattering of a nano-crystal/illuminated nano-region of size Md, where d is the crystalline unit cell, to have enough sampling points to interpolate $I(u)$ everywhere *via* the GST we need to have $N = 2M$, due to the fact that the auto-correlation function of the nano-crystal/illuminated nano-region has a doubled size. In other words, we need $2M$ irregular samples in the diffraction pattern to compensate for the lack of diffracted intensity information due to noise, as shown in Fig. 9. In the figure we report a schematic comparison between the unit-cell Nyquist sampling ($1/d$), the nano-crystal/illuminated nano-region diffracted intensity Nyquist sampling ($1/2Md$) (dashed vertical lines) and the nano-crystal/illuminated nano-region diffracted intensity measured at an S oversampling (solid vertical lines). The horizontal solid line schematically denotes the noise level that could prevent the experimental measurement of many nano-crystal/illuminated nano-region diffracted intensities at the Nyquist sampling ($1/2Md$). But if the oversampling ratio S is sufficiently high the lack of nano-crystal/illuminated nano-region diffracted intensities at the Nyquist sampling ($1/2Md$) below the noise level can be compensated by the further diffracted intensity measurements which are possible just due to the S oversampling. In turn, these new diffracted intensities can be considered as an irregular/interlaced (see Appendix *A*) sampling of the diffraction pattern, when compared to the nano-crystal/illuminated nano-region diffracted intensity $1/2Md$ sampling. This finding gives the possibility, *via* the GST [equation (11)], of calculating continuously everywhere the diffracted intensity. In this way the experimental EDI/KEDI diffraction pattern could contain all information needed to perform a reliable phase-retrieval process. In other words, if the oversampling ratio is very high, the support has a very small size with respect to the whole matrix of points measured at the detector. The larger is S, the smaller would be the number of object points characterized by a scattering different from zero, the smaller would be the number of diffracted intensities that have to be larger than the noise level in order for it to be possible to reliably retrieve phase information. Thus, suitable oversampling ratios could completely compensate for the loss of information about both weaker IBD intensities and phases. Let us note that the explanation of the oversampling method by using enough independent equations *versus* the number of unknown variables was first suggested by Miao *et al.* (1998), who also first proposed the oversampling ratio as a criterion to evaluate the information content in the coherent diffracted patterns. Furthermore, the unknown diffraction intensities, lost due to the noise, are the weaker intensities and the approximation with zero for these weak diffraction intensities is already a good approximation, often sufficient to realize efficient phase retrievals, as shown in §2. As a rule of thumb, one should have at least as many non-null diffracted intensities in a KEDI map as the unknowns (values of the projected atomic potential inside the support and unknown phases). But the possibility to know *a priori* the object support and the low-resolution phases of the scattering function from the HRTEM image allows phase information extension from low to high space resolution, instead of a true *ab initio* phasing process. This finding offers the possibility of finding a reliable phase solution even in conditions for which

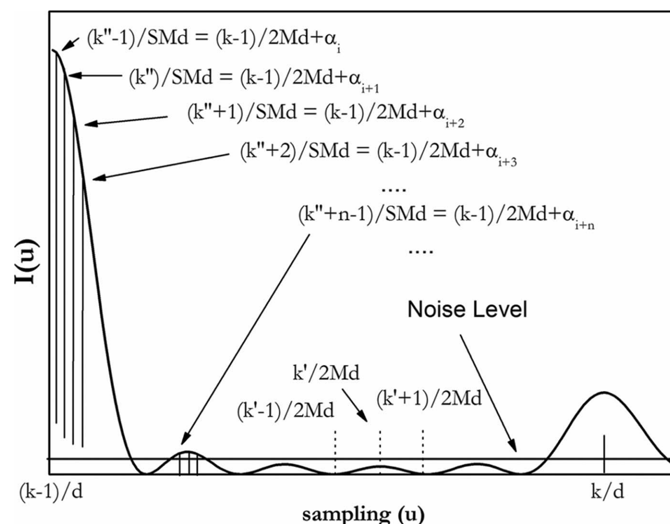

Figure 9
Schematic comparison between the unit-cell Nyquist sampling ($1/d$), the nano-crystal/illuminated nano-region diffracted intensity Nyquist sampling ($1/2Md$) (dashed vertical lines) and the nano-crystal/illuminated nano-region diffracted intensity measured with an S oversampling (solid vertical lines). The horizontal solid line schematically denotes the noise level that could prevent experimental measurement of many nano-crystal/illuminated nano-region diffracted intensities at the Nyquist sampling ($1/2Md$).

in Fourier space the lack of information in principle should not permit one to reconstruct any phase information. Actually, this missing information in Fourier space in KEDI experiments could be, at least partially, compensated for by further information available in real space, as shown in the main text. All the above elements indicate that EDI/KEDI phase problems could have a reliable solution even if its uniqueness could not be guaranteed from a mathematical point of view, just as happens in X-ray crystallography.

The extension of the GST approach to a two-dimensional function is beyond the scope of the present work. Instead, in the main text, simulated data mark how the result of the phasing process can lead to the correct reconstruction of the object with enough accuracy.

APPENDIX *C*
The complex scattering function in EDI/KEDI experiments

This appendix aims to show that in the EDI/KEDI phase problem, for non-null crystal tilt angles and in kinematical scattering conditions, the phase of the complex $U(\mathbf{r})$ scattering function would have practically no information about the unknown sample's atomic structure. Indeed, in weak phase object approximation (Hirsch *et al.*, 1997; Spence, 2003), the electron wavefunction $\psi(\mathbf{r})$ is related to the specimen electrostatic crystal potential $V(\mathbf{r})$ by $\psi(\mathbf{r}) \cong 1 + i\pi\lambda U(\mathbf{r})$, where $U(\mathbf{r})$ equals $2meV(\mathbf{r})/h^2$, with m the relativistic mass of the electron, λ its wavelength and e its charge. In reciprocal space the diffracted intensity in the kinematical approximation (Hirsch *et al.*, 1997) can be written as

$$I(\mathbf{k}) \propto (\pi\lambda)^2 \left|F(\mathbf{k})\right|^2, \tag{15}$$

apart from a constant term. Here $F(\mathbf{k})$ is the structure factor corresponding to the scattering potential $U(\mathbf{r})$.

In general, EDI/KEDI diffraction patterns do not satisfy Friedel's law (Kambe, 1967). Thus, they are not centrosymmetric patterns. The FT^{-1} of $I(\mathbf{k})$ gives, for the convolution theorem of FT, the autocorrelation function $A(\mathbf{r}) = \mathrm{FT}^{-1}[I(\mathbf{k})]$. For a centrosymmetric $I_{cs}(\mathbf{k})$ pattern, $A(\mathbf{r})$ is real and positive. For a non-centrosymmetric $I(\mathbf{k})$ pattern $A(\mathbf{r})$ is a complex Hermitian function:

$$\begin{aligned} A(\mathbf{r}) &= \textstyle\int \exp(i\mathbf{k}\cdot\mathbf{r})I(\mathbf{k})\,\mathrm{d}\mathbf{k} \\ &\equiv \textstyle\int \exp(i\mathbf{k}\cdot\mathbf{r})I_{cs}(\mathbf{k})\,\mathrm{d}\mathbf{k} + \int \exp(i\mathbf{k}\cdot\mathbf{r})\Delta I(\mathbf{k})\,\mathrm{d}\mathbf{k} \\ &= A_{cs}(\mathbf{r}) + i\textstyle\int \sin(\mathbf{k}\cdot\mathbf{r})\Delta I(\mathbf{k})\,\mathrm{d}\mathbf{k}. \end{aligned} \tag{16}$$

In equation (16) the coherent diffracted intensity has been divided into its symmetric $[I_{cs}(\mathbf{k})]$ and anti-symmetric $[\Delta I(\mathbf{k})]$ contributions to show that the imaginary part of $A(\mathbf{r})$ depends only on the non-centrosymmetric part of the diffraction pattern. Indeed $A_{cs}(\mathbf{r})$ is real and positive.

The non-centrosymmetric component of the EDI/KEDI diffraction pattern due to absorption derives from inelastic interactions such as phonon scattering, plasmon scattering and single electron excitations from inner atoms (Radi, 1970; Humphreys & Hirsh, 1968). All these effects contribute very little only to the complex part of the phase-retrieved object scattering function in EDI experiments. It should be noted that the complex part of the EDI phase-retrieved object scattering function is only a few percent of the real part (Huang *et al.*, 2009; De Caro *et al.*, 2010). Moreover, the cross section from phonon scattering is rather peaked at the atom cores and the corresponding absorption effects can be described by introducing a complex potential where the imaginary part is proportional to the real part (Humphreys & Hirsh, 1968; Wang *et al.*, 2010). Thus,

$$U(\mathbf{r}) = U_{\mathrm{R}}(\mathbf{r}) + iU_{\mathrm{I}}(\mathbf{r}) \cong U_{\mathrm{R}}(\mathbf{r}) + i\alpha U_{\mathrm{R}}(\mathbf{r}), \tag{17}$$

with α very small, of the order of 0.01–0.05 for many atomic species with atomic number up to Fe (Humphreys & Hirsh, 1968). For example, for silicon at 200 keV $\alpha \simeq 0.029$. As a consequence of this peculiar property of high-energy electron inelastic scattering, from equation (17) it follows that for null tilt axes (*i.e.* perfectly aligned samples in the considered zone axis) the autocorrelation function of $U(\mathbf{r})$ would be well approximated by

$$A(\mathbf{r}) \cong (1+\alpha^2)A_{\mathrm{R}}(\mathbf{r}) \cong A_{\mathrm{R}}(\mathbf{r}), \tag{18}$$

i.e. it can be well approximated by a real function. In other words, almost all the asymmetry of the electron diffraction pattern can be ascribed, in kinematical scattering conditions, to misalignment of the crystal with respect to the exact zone axes. Consequently, for non-null crystal tilt angles and in kinematical scattering conditions, the phase of the complex $U(\mathbf{r})$ scattering function does not carry further information about the unknown sample's atomic structure, which is not yet contained in $U_{\mathrm{R}}(\mathbf{r})$. This is true until the product of the tilt angle ε and crystal thickness t is small and the phases of the structure factors are not affected by the tilt (Zuo, 1995, p. 94). Only their modules are affected, breaking the almost-perfect Friedel symmetry [*i.e.* $I(\mathbf{k}) = I(-\mathbf{k})$] between symmetry-related diffraction beams. Indeed it can be shown that if the product $\varepsilon \times t$ is less than the spacing corresponding to the in-plane scattering vector value $\mathbf{k}$, only the amplitude $[I(\mathbf{k})]^{1/2}$ is attenuated (Zuo, 1995, pp. 50–55). For example, for a 5 nm sample thickness and a mis-tilt ε of about 0.5°, none of the diffracted beams, down to 44 pm spacing, would be affected by the phase of the complex scattering function. Therefore, in the presence of a weak phase object the measured diffraction pattern – before the phasing process – could also be made centrosymmetric by using the procedure described in Zuo (1995, pp. 50–55), without any lack of structural information about the unknown projected potential, and a real-object constraint could be safely applied during phase retrieval.

Conversely, as underlined also by Huang *et al.* (2007), for an object potential stronger than the weak phase object the dynamical diffraction effects would lead to a complex object function. In this case, any real-object constraint in inverting the diffraction pattern would not be applicable. However, it should be noted that in the presence of strong dynamical effects all diffracted intensities would be strongly affected and they would no longer be directly related to the FT of the projected atomic potential. Therefore its reconstruction,

through phase retrieval of a dynamical EDI/KEDI pattern, would fail not only because the real-object constraint is not valid, but mainly because the measured diffraction pattern does not contain any information directly proportional to the FT modulus of the object scattering function. Nevertheless, as shown in §3, the object scattering function can be correctly retrieved even in the presence of a small amount of dynamical effects and only when the dynamical effects produce strong intensity variation can the phasing not be safely performed.

APPENDIX *D*
Coherence properties of the incident beam in a KEDI experiment

The evolution of the temporal and spatial coherence properties of a propagating wavefield can be described by means of the mutual coherence function (MCF) formalism, in a paraxial approximation, convolving the complex amplitude $a(\mathbf{s})$ of the wavefield, emitted by the source in a generic point $\mathbf{s}$, with the Fresnel propagator (Shina *et al.*, 1998):

$$J(\mathbf{r}_\perp, \mathbf{r}'_\perp) = \frac{1}{iq\lambda}\iint \mathrm{d}\mathbf{s}\,\mathrm{d}\mathbf{s}'a(\mathbf{s})a^*(\mathbf{s}')S(\mathbf{s}-\mathbf{s}') \times \exp\left\{\frac{i\pi\left[(\mathbf{s}-\mathbf{r}_\perp)^2-(\mathbf{s}'-\mathbf{r}_\perp{}')^2\right]}{q\lambda}\right\}. \tag{19}$$

Equation (19) describes the interference of wavefields emitted by a source and propagated to a distance q. The function $J(\mathbf{r}, \mathbf{r}')$ is the mutual optical intensity (MOI) and describes how the lateral spatial coherence of the propagating wavefield evolves at different distances q; the symbol * denotes the complex conjugate; the vectors $\mathbf{r} = (\mathbf{r}_{||}, \mathbf{r}_\perp)$ and $\mathbf{r}' = (\mathbf{r}_{||}{}', \mathbf{r}_\perp{}')$ have been decomposed in parallel and perpendicular components, respectively, with respect to the optical axis; $a(\mathbf{s})$ is the *complex* wavefield amplitude in the source plane, whose squared modulus gives the total beam intensity emitted by the source area; $S(\mathbf{s}-\mathbf{s}')$ is the coherence factor between different points of the source, and describes the spatial coherence of the source at its exit surface. Equation (19) holds for quasi-monochromatic sources if the propagation distance q is much larger than both the source size and the maximum values of $|\mathbf{r}_\perp - \mathbf{r}_\perp{}'|$ in any plane perpendicular to the optical axis.

In the incoherent limit one has $S(\mathbf{s}-\mathbf{s}') \to \delta(\mathbf{s}-\mathbf{s}')$, *i.e.* the source coherence factor can be assimilated to a Dirac delta function. Under this assumption, from equation (19) one has

$$J(\mathbf{r}_\perp, \mathbf{r}'_\perp) = \frac{1}{iq\lambda}\int \left|a(\mathbf{s})\right|^2 \exp\left\{\frac{i\pi\left[\mathbf{r}_\perp^2-\mathbf{r}_\perp{}'^2-2\mathbf{s}\cdot\left(\mathbf{r}_\perp-\mathbf{r}'_\perp\right)\right]}{q\lambda}\right\}\mathrm{d}\mathbf{s}. \tag{20}$$

In the far-field limit, the Fresnel propagator effects disappear and equation (20) gives just the Van Cittert–Zernike theorem which relates the angular distribution of the wavefield impinging onto the sample to the FT of the physical source square *modulus* amplitude $|a(\mathbf{r})|^2$ (Born & Wolf, 1991).

Thus, the measured intensity in a KEDI experiment $I_{\rm KEDI}(\mathbf{k})$, scattered by the sample illuminated by a nano-sized beam, would be given by a convolution product (Kawahara *et al.*, 2010):

$$I_{\rm KEDI}(\mathbf{k}) \propto I_{\rm pw}(\mathbf{k}) \otimes I_s(\mathbf{k}). \tag{21}$$

Here $\otimes$ denotes convolution, $I_s(\mathbf{k})$ is the incident beam intensity and $I_{\rm pw}(\mathbf{k})$ the scattered intensity that would be obtained for an impinging plane wave. This convolution is related to the finite size of the incident beam in real space, which acts as a 'keyhole', which goes to zero out of the sample illuminated region.

It should be noted that equation (21) implies that it is not necessary to know the incident illumination function in modulus and phase, such as for ptychography (Faulkner & Rodenburg, 2004; Thibault *et al.*, 2008; Dierolf *et al.*, 2010) or in Fresnel X-ray keyhole CDI (Abbey *et al.*, 2008), but it is sufficient to know only the intensity of the electron probe. This finding is verified when the spatial coherence is developed through wave propagation and when we are dealing with a Fraunhofer diffraction geometry. This result is a direct consequence of the Van Cittert–Zernike theorem (Born & Wolf, 1991).

References

Abbey, B., Nugent, K. A., Williams, G. J., Clark, J. N., Peele, A. G., Pfeifer, M. A., De Jonge, M. & McNulty, I. (2008). *Nature (London)*, **4**, 394–398.

Banhart, F. (1994). *Ultramicroscopy*, **56**, 233–240.

Barakat, R. & Newsam, G. (1984). *J. Math. Phys.* **25**, 3190–3193.

Bates, R. H. T. (1982). *Optik*, **61**, 247–262.

Bates, R. H. T. (1984). *Comput. Vision Graph. Image Process.* **25**, 205–217.

Born, M. & Wolf, E. (1991). *Principles of Optics*, VI ed., p. 510. Oxford: Pergamon.

Caliandro, R., Carrozzini, B., Cascarano, G. L., De Caro, L., Giacovazzo, C. & Siliqi, D. (2005). *Acta Cryst.* D**61**, 556–565.

Carlino, E. (2008). *Beam Injection Based Nanocharacterization of Advanced Materials*, edited by G. Salviati, T. Sekiguchi, S. Heun & A. Gustafsson, p. 223. Kerala: Research Signpost.

Carlino, E. & Grillo, V. (2006). *Arch. Metall. Mater.* **51**, 23–32.

De Caro, L., Carlino, E., Caputo, G., Cozzoli, P. D. & Giannini, C. (2010). *Nat. Nanotech.* **5**, 360–365.

Dierolf, M., Menzel, A., Thibault, P., Schneider, P., Kewish, C. M., Wepf, R., Bunk, O. & Pfeiffer, F. (2010). *Nature (London)*, **467**, 436–439.

Faulkner, H. M. & Rodenburg, J. M. (2004). *Phys. Rev. Lett.* **93**, 023903.

Fienup, J. R. (1982). *Appl. Opt.* **21**, 2758–2769.

Fienup, J. R. (1987). *J. Opt. Soc. Am. A*, **4**, 118–127.

Hirsch, P. B., Howie, A., Nicholson, R. B., Pashley, D. W. & Whelan, M. J. (1997). *Electron Microscopy of Thin Crystals*, p. 195. Malabar: Krieger.

Hosemann, R. & Bagchi, S. N. (1953). *Acta Cryst.* **6**, 318–325.

Huang, W. J., Jiang, B., Sun, R. S. & Zuo, J. M. (2007). *Ultramicroscopy*, **107**, 1159–1170.

Huang, W. J., Zuo, J. M., Jiang, B., Kwon, K. W. & Shim, M. (2009). *Nat. Phys.* **5**, 129–133.

Humphreys, C. J. & Hirsh, P. B. (1968). *Philos. Mag.* **18**, 115–122.

Kambe, K. (1967). *Z. Naturforsch. Teil A*, **22**, 422–426.

Kawahara, K., Gohara, K., Maehara, Y., Dobashi, T. & Kamimura, O. (2010). *Phys. Rev. B*, **81**, 081404(R).
Liu, Z.-C., Xu, R. & Dong, Y.-H. (2012). *Acta Cryst.* A**68**, 256–265.
Marchesini, S. (2007). *Rev. Sci. Instrum.* **78**, 011301.
Marchesini, S., He, H., Chapman, H. N., Hau-Riege, S., Noy, A., Howells, M., Weierstall, U. & Spence, J. C. H. (2003). *Phys. Rev. B*, **68**, 140101(R).
Marks, R. J. II (1991). *Introduction to Shannon Sampling and Interpolation Theory*. New York: Springer-Verlag.
Miao, J., Charalambous, P., Kirz, J. & Sayre, D. (1999). *Nature (London)*, **400**, 342–344.
Miao, J., Ishikawa, T., Anderson, E. K. & Hodgson, K. O. (2003). *Phys. Rev. B*, **67**, 174104.
Miao, J., Ishikawa, T., Shen, Q. & Earnest, T. (2008). *Annu. Rev. Phys. Chem.* **59**, 387–410.
Miao, J., Sayre, D. & Chapman, H. N. (1998). *J. Opt. Soc. Am. A*, **15**, 1662–1669.
Millane, R. P. (1996). *J. Opt. Soc. Am. A*, **13**, 725–734.
Nugent, K. A. (2010). *Adv. Phys.* **59**, 1–99.
Papoulis, A. (1977). *IEEE Trans. Circuits Syst.* **CAS-24**, 652–654.
Papoulis, A. (1986). *Systems and Transforms with Applications in Optics*. Malabar: McGraw-Hill.
Radi, G. (1970). *Acta Cryst.* A**26**, 41–56.
Sayre, D. (1952*a*). *Acta Cryst.* **5**, 843.
Sayre, D. (1952*b*). *Acta Cryst.* **5**, 60–65.
Shannon, C. E. (1949). *Proc. Inst. Radio Eng. (NY)*, **37**, 10–41.
Shina, S. K., Tolan, M. & Gibaud, A. (1998). *Phys. Rev. B*, **57**, 2740–2758.
Spence, J. C. H. (2003). *High-Resolution Electron Microscopy*. Oxford University Press.
Thibault, P., Dierolf, M., Menzel, A., Bunk, O., David, C. & Pfeiffer, F. (2008). *Science*, **321**, 379–382.
Van Dyck, D. (1992). *Electron Microscopy in Materials Science*, edited by P. G. Merli & M. Vittori Antisari, pp. 193–268. Singapore: World Scientific.
Walther, A. (1963). *Opt. Acta*, **10**, 41–49.
Wang, A., Chen, F. R., Van Aert, S. & Van Dyck, D. (2010). *Ultramicroscopy*, **110**, 527–534.
Whitehead, L. W., Williams, G. J., Quiney, H. M., Nugent, K. A., Peele, A. G., Paterson, D., de Jonge, M. D. & McNulty, I. (2008). *Phys. Rev. B*, **77**, 104112.
Williams, G. J., Quiney, H. M., Dhal, B. B., Tran, C. Q., Nugent, K. A., Peele, A. G., Paterson, D. & de Jonge, M. D. (2006). *Phys. Rev. Lett.* **97**, 025506.
Williams, G. J., Quiney, H. M., Peele, A. G. & Nugent, K. A. (2007). *Phys. Rev. B*, **75**, 104102.
Xiao, X. & Shen, Q. (2005). *Phys. Rev. B*, **72**, 033103.
Zuo, J. M., Vartanyants, I., Gao, M., Zhang, R. & Nagahara, L. A. (2003). *Science*, **300**, 1419–1421.
Zuo, X. D. (1995). Doctoral Dissertation, Stockholm University. *Chem. Commun. Stockholm Univ.* No. 5.